UCSF

Title

Perfusion and diffusion sensitive 13C stimulated-echo MRSI for metabolic imaging of cancer

Permalink

https://escholarship.org/uc/item/17g472ph

Journal

Magnetic Resonance Imaging, 31(5)

ISSN

0730-725X

Authors

Larson, Peder EZ
Hurd, Ralph E
Kerr, Adam B
et al.

Publication Date

2013-06-01

DOI

10.1016/j.mri.2012.10.020

Peer reviewed

Perfusion and Diffusion Sensitive 13C Stimulated-echo MRSI for Metabolic Imaging of Cancer

Peder E. Z. Larson[1], **Ralph E. Hurd**[2], **Adam B. Kerr**[3], **John M. Pauly**[3], **Robert A. Bok**[1], **John Kurhanewicz**[1], and **Daniel B. Vigneron**[1]

[1]Department of Radiology and Biomedical Imaging, University of California - San Francisco, San Francisco, California

[2]Applied Science Laboratory, GE Healthcare, Menlo Park, California

[3]Magnetic Resonance Systems Research Laboratory, Department of Electrical Engineering, Stanford University, Stanford, California

Abstract

Metabolic imaging with hyperpolarized [1-^{13}C]-pyruvate can rapidly probe tissue metabolic profiles in vivo and has been shown to provide cancer imaging biomarkers for tumor detection, progression, and response to therapy. This technique uses a bolus injection followed by imaging within 1–2 minutes. The observed metabolites includes vascular components and their generation is also influenced by cellular transport. These factors complicate image interpretation, especially since [1-^{13}C]lactate, a metabolic product that is a biomarker of cancer, is also produced by red blood cells. It would be valuable to understand the distribution of metabolites between the vasculature, interstitial space, and intracellular compartments. The purpose of this study was to better understand this compartmentalization by using a perfusion and diffusion-sensitive stimulated-echo acquisition mode (STEAM) MRSI acquisition method tailored to hyperpolarized substrates. Our results in mouse models showed that among metabolites, the injected substrate ^{13}C-pyruvate had the largest vascular fraction overall while ^{13}C-alanine had the smallest vascular fraction. We observed a larger vascular fraction of pyruvate and lactate in the kidneys and liver when compared to back muscle and prostate tumor tissue. Our data suggests that ^{13}C-lactate in prostate tumor tissue voxels was the most abundant labeled metabolite intracellularly. This was shown in STEAM images that highlighted abnormal cancer cell metabolism and suppressed vascular ^{13}C metabolite signals.

Keywords

Hyperpolarized C-13; metabolic imaging; stimulated-echo acquisition mode (STEAM); perfusion contrast; diffusion spectroscopy; TRAMP; prostate cancer

Introduction

Using injected hyperpolarized [1-^{13}C]pyruvate for *in vivo* metabolic imaging has been recently demonstrated for feasibility and to have potential clinical value (1–15). These studies have been made possible by the development of methods utilizing Dynamic Nuclear Polarization (DNP) and rapid dissolution techniques that provide a polarization increase of over 40,000 for [1-^{13}C]pyruvate while producing an injectable solution with physiologic pH, osmolarity, and temperature (1,2). Following injection, the conversion of pyruvate to its metabolic products of lactate, alanine, and bicarbonate *in vivo* can be detected in sub-minute acquisition times. This is of particular value for cancer imaging in which the metabolic profile has been shown to distinguish between normal and diseased tissues in preclinical animal models (3–5,8,10–12). This metabolic information has also been used to monitor cardiac function, and reperfusion in both the heart and lung following ischemia (6,7,9,15).

In vivo imaging with hyperpolarized substrates requires rapid and efficient MR imaging techniques because the high polarization is irreversibly lost due to T_1 relaxation to thermal equilibrium and T_2 relaxation following any RF excitation. This also requires that data be acquired within 1–2 minutes after the bolus injection, and metabolites are observed in the vasculature in addition to the tissues or organs of interest. Furthermore, the [1-^{13}C]lactate generated following a [1-^{13}C]pyruvate injection - a potential biomarker because it is elevated in tumors - is both transported out of cells and also generated in the blood by erythrocytes, which have detectable lactate dehydrogenase (LDH) activity (16, 17). High [1-^{13}C]lactate levels observed in kidneys are presumably predominantly from blood flow into the organ and excretion of lactate, which is not an accurate reflection of metabolism within the kidney. The localization of metabolites can be precisely studied in a setting where flow and perfusion can be controlled such as with cells in a bioreactor (18,19). In vivo, the signal from flowing metabolites can confound the interpretation of metabolic imaging results. One approach proposed to address this problem is to use a spectral-spatial suppression pulse applied across the chest cavity to saturate lactate and alanine flowing through the heart and lungs (20), which provides qualitative contrast improvements but is not a quantitative measure of perfusion. Another approach is to use a subsequent Gadolinium injection to shorten the T_1 of vascular and extracellular metabolites, which then isolates the ^{13}C signal to intracellular components (21). It has also been shown that flowing metabolites can be suppressed by using the crusher gradients around spin-echo pulses (22), as done in spin-echo diffusion-weighted imaging.

The purpose of this study was to examine the compartmentalization of metabolites at the short interval after injection of hyperpolarized [1-^{13}C]pyruvate. To investigate this compartmentalization, we developed and applied a perfusion and diffusion sensitive stimulated-echo acquisition mode (STEAM) MRSI acquisition method tailored for hyperpolarized substrates. Stimulated echoes are inherently sensitive to motion, a characteristic which has been utilized for cardiac (23, 24), diffusion (25, 26), and spectroscopic imaging (27). The contrast from motion sensitivity includes both perfusion processes (macroscopic scale) and molecular diffusion (microscopic scale) (28, 29). This motion sensitivity can also be achieved in diffusion-weighted spin-echo sequences, but STEAM allows for larger encoding strengths to observe a broader range of perfusion and diffusion contrast. Because the encoding strength (*b*-value) is proportional to γ^2, this is especially important in ^{13}C, which has a gyromagnetic ratio, γ, that is about 4-times smaller than that of [1]H.

Compartmentalization of metabolites has been performed on cell cultures with diffusion-weighted ^{1}H MRS (30–38). These studies demonstrated diffusion-weighting can be used for separation of intracellular metabolites. However, their approaches cannot be directly applied

to this study because they were not designed for hyperpolarized experiments, were not performed within the limitations of a clinical MRI system, and did not include imaging. The STEAM MRSI approach used in this study addresses all of these concerns.

A stimulated-echo approach with frequency-selective tagging of the hyperpolarized [1-^{13}C]pyruvate substrate has been used to isolate [1-^{13}C]lactate and [1-^{13}C]alanine signals derived exclusively from the substrate (39). We have also presented initial results using a perfusion-sensitive super stimulated-echo preparation approach with hyperpolarized [1-^{13}C]pyruvate in normal (N = 4) and transgenic prostate tumor bearing mice (TRAMP, N = 4) (40). This study showed improved tumor lactate delineation as reflected by a significant increase in both the [1-^{13}C]lactate to [1-^{13}C]pyruvate ratio within the tumors and the ratio of peak tumor [1-^{13}C]lactate to peak kidney/liver [1-^{13}C]lactate, indicating that the [1-^{13}C]lactate observed in kidney and liver tissue had a larger vascular fraction than the [1-^{13}C]lactate within tumor tissue. Based on these promising results, we acquired STEAM MRSI with varying encoding strengths (b-values) in mice (N = 6 normal and N = 8 prostate tumor) in this study to better characterize the metabolite compartmentalization in the liver, kidneys, muscle, and prostate tumor tissue.

Theory

The motion sensitivity of stimulated-echoes is due to the gradient encoding between the initial 90-90 pulses, which are refocused after the mixing time (TM) but only for stationary spins. The sensitivity to motion is determined by the b-value (25, 26). With the rapid STEAM pulse sequence (41) (Figure 1a), phase encodes are acquired at different mixing times because a single encoding step is sampled repeatedly. This sequence has a b-value that varies across k-space:

$$b(\vec{k})=(\gamma G_{STEAM}\delta)^2(\Delta(\vec{k})-\delta/3) \quad (1)$$

$$=(\gamma G_{STEAM}\delta)^2(TM+n(\vec{k})TR+2\delta/3), \quad (2)$$

where G_{STEAM} and δ are the STEAM encoding gradient amplitude and duration, respectively (neglecting gradient ramps), $\Delta(\vec{k})$ is the separation between the dephasing and rephasing diffusion gradients, and $n(\vec{k})$ represents the phase encode ordering. For the concentric ordering used in this study, intravoxel motion during the $n(\vec{k})$ phase encodes will lead to isotropic spatial blurring. We characterized the encoding strength for this sequence using point spread function (PSF) analysis by first computing

$$PSF(\vec{x}, D)=\mathscr{F}(\exp(-b(\vec{k})D)) \quad (3)$$

for the concentric phase encode ordering, where D is the apparent diffusion coefficient (ADC). The PSFs in Figure 2 show resulting losses in both the signal amplitude and spatial resolution due to diffusion. We then calculated an effective b-value by assuming exponential decay of the peak PSF amplitude:

$$\widehat{b}=\frac{-1}{D_w}\ln PSF(\vec{x}=0, D_w) \quad (4)$$

using the diffusivity of protons in free water, $D = D_w = 2.3 \times 10^{-3}$ mm^2/s. The drawback to this characterization is that the PSF amplitude is not exactly exponential with respect to D.

However, across the range of estimated ADC values in Table 2, the resulting variation in the effective b-values is   15%. Thus we believe this is reasonable approximation.

The motion sensitivity of STEAM can result in both perfusion and diffusion contrast as well as signal loss due to bulk motion. It has been demonstrated that lower b-value encodings ($b < 200$ s/mm^2) are primarily perfusion sensitive, while the higher b-value encodings ($b > 500$ s/mm^2) are also sensitive to restricted diffusion (28, 29). This framework is used in intravoxel incoherent motion (IVIM) MR imaging to extract a vascular fraction or a "pseudo-diffusion" coefficient (macroscopic-scale processes of blood flow in vasculature) and the conventional ADC (microscopic processes of molecular diffusion) (29) to provide information about the microcirculatory flow and capillary networks.

Methods

MRSI Pulse Sequence

Hyperpolarization is a substantial perturbation from thermal equilibrium so there is no steady-state for hyperpolarized compounds. Thus, any RF excitation alters the magnetization profile for all subsequent acquisitions. Our approach for 3D STEAM MRSI, shown in Figure 1a, was to use a single encoding step followed by multiple excitation and acquisitions that progressively sample the longitudinally encoded magnetization similarly to the approach proposed in (41). For hyperpolarized studies, carbon-13 compounds suitable for dissolution DNP and *in vivo* imaging have relatively long T_1 values ($\approx 20 - 40 s$ for [1-^{13}C]pyruvate, [1-^{13}C]lactate, and [1-^{13}C]alanine at 3T), which allows for relatively long mixing times (*TM*) of several seconds to be used without substantial magnetization loss.

The excitation used non-selective 264 μs rectangular pulses with a progressive flip angle scheme (42) that efficiently utilizes the encoded magnetization and provides uniform weighting across phase encodes assuming no T_1 decay during the acquisition. An echo-planar spectroscopic imaging (EPSI) readout was used for simultaneous acquisition of spectral and spatial data. The readout gradient consisted of symmetric positive and negative lobes, all of which were utilized for data collection to increase the SNR efficiency (43). Ramp sampling was also utilized to further improve the efficiency. Spectroscopic imaging from the positive and negative lobes were reconstructed separately with 10 Hz spectral apodization, and their magnitudes were summed to form the final images. The EPSI gradient was 102.08 ms with a spectral resolution of 9.79 Hz, 581 Hz spectral bandwidth, 18 spatial points, and a minimum resolution of 4.45 mm.

Experiments

All animal studies were carried out under a protocol approved by the Institutional Animal Care and Use Committee. Experiments were performed on a GE 3T clinical MRI system (GE Healthcare, Waukesha, WI, USA) with 40 mT/m, 150 mT/m/ms gradients and a broadband RF amplifier. A custom built, dual-tuned mouse birdcage coil was used for RF transmission and signal reception (44). A compound consisting of neat [1-^{13}C] pyruvic acid (14.2 M) and the trityl radical OX063 (15 mM) (GE Healthcare, Oslo, Norway) was polarized in a HyperSense DNP system (Oxford Instruments, Abingdon, UK) at 3.35 T and a temperature of 1.4° K. The hyperpolarized pyruvate was dissolved to a concentration of 80 mM in a mixture of distilled water, 80 mM NaOH, 40 mM Tris, and 0.3 mM EDTA. 350 μL of this solution was injected into the animal over 12 seconds. An aliquot of this solution was taken and injected into a polarimeter to measure the percent polarization, which we estimate to have a less than 10% error. Another aliquot was used to monitor the pH. The animals were placed on a 37°C heating pad in the RF coil, and anesthesia was maintained by a

continual delivery of isoflurane (1–1.5%) with oxygen (1 liter/min). Respiratory rate and skin color were monitored by periodic visual inspection.

In order to characterize the STEAM contrast experiments were performed on normal mice as well as on a transgenic adenocarcinoma of mouse prostate (TRAMP) mouse model, four mice with early-stage tumors, three with intermediate-stage tumors, and one with a late-stage tumor. Tumor stage was evaluated by T2-weighted proton MRI. Two 3D MRSI experiments were acquired with each animal utilizing separate hyperpolarized injections: (1) free-induction decay (FID) acquisition ("control", $b = 0$, Figure 1b, Eq. 6) and (2) STEAM (Figure 1a, Eq. 5). Based on reproducibility studies in normal rats (45), the distribution of metabolites is expected to be relatively consistent between injections. Imaging was initiated 35 seconds following the start of the injection with $5 \times 5 \times 5$mm (0.125 cm^3) resolution, $8 \times 8 \times 16$ matrix size, $TE_S = 20$ ms (STEAM), $TE_F = 10$ ms (FID), TR = 125 ms, a concentric phase encode ordering, and 8 sec acquisition time. The STEAM encoding gradient was applied identically on all 3 axes. In the FID experiments, a delay of TM was inserted into the acquisition so that the data were acquired at the same time relative to injection in both experiments. All experimental parameters are listed in Table 1, and the $\hat{b}$ values are noted in all figures. Because of the relatively long TM used, the phase encoding gradients had a less than 1% effect on $\hat{b}$.

Analysis

We modeled the signal behavior of our STEAM acquisition as

$$S_{STEAM} = S_0 \cdot \frac{1}{2} A_{STEAM} \exp(-TE_S / T_2) \cdot \exp(-\widehat{bD}). \quad (5)$$

This includes the nominal signal (S_0), the 50% inherent STEAM signal loss, additional losses (A_{STEAM}) due to imperfect RF pulses and bulk motion blurring, T_2 decay, and perfusion/diffusion sensitivity ($\exp(-\hat{b}\hat{D})$). The FID acquisition was used as a "control" because it provides an estimate of S_0:

$$S_{FID} = S_0 \exp(-TE_F / T_2^*) \quad (6)$$

The data were analyzed by computing the STEAM:control ratio in each animal

$$S_{STEAM} / S_{FID} = \frac{1}{2} A_{STEAM} \exp(-TE_S / T_2 + TE_F / T_2^*) \cdot \exp(-\widehat{bD}). \quad (7)$$

Experiments with different $\hat{b}$-values across all animals were fit with a non-linear exponential regression to the model in Eq. 7, yielding gross estimates of the intercept term and $\hat{D}$ in different organs.

The resulting intercept includes losses due to imperfect RF pulses and motion blurring in A_{STEAM}, and relaxation differences. We estimate that the effects of imperfect RF pulses were consistent between metabolites and tissues because the RF coil was a birdcage that is relatively homogeneous in the region encompassing the liver to the prostate tumors. The effect of T_2 decay on the ratio can be estimated using measured relaxation times *in vivo* for hyperpolarized [1-^{13}C]pyruvate and its metabolites of $T_2 > 100$ ms (46), and our measurements of $T_2^* \geq 50$ using *in vivo* spectral linewidths. For these values, the relaxation term has a range of $0.90 < \exp(-TE_S / T_2 + TE_F / T_2^*) < 1.23$, which approaches 1 as T_2^* and T_2 increase. (The lower limit is reached with ideal homogeneity and the minimum relaxation

time, $T_2^*=T_2=100$, and the upper limit when $T_2^* \ll T_2$). When comparing metabolites within a tissue, this range will be even smaller since they will experience the same B_0 inhomogeneity and thus will have similar T_2^* values. The remaining metabolite or tissue differences in the intercept fit are due to blurring losses from macroscopic motion such as respiration, cardiac motion, or blood flow. For *in vivo* blood velocities (0.7 mm/s for humans, higher in mice) the blood displacement would be similar to or greater than the spatial encoding period (1.82 or 0.571 mm for $\hat{b}$ = 58.4 or 513.3 s/mm², respectively) over the 1 sec mixing times used. Consequently, macroscopic blood flow will be substantially suppressed, which is accounted for in A_{STEAM}.

A single effective diffusion coefficient ($\hat{D}$) was used in the model to provide an estimate of the diffusion-weighting. Previous work (29) proposed a joint perfusion and diffusion framework that includes both the ADC, D, which reflects the microscopic process of molecular diffusion, and either a "pseudodiffusion" coefficient, D^*, to reflect the macroscopic scale processes of blood flow in vasculature or a vascular fraction f. In our experiments, macroscopic flow will be largely suppressed because of the long mixing times used and will affect A_{STEAM} as described above. Therefore, we expect $\hat{D}$ will primarily reflect microscopic diffusion while the intercept of the exponential fits will be primarily due to macroscopic blood flow and bulk motion.

Metabolite peak heights were used in the data analyses and image overlays. To create the color overlays, the MRSI peak heights (5 × 5 × 5 mm) were coregistered and resampled to the proton anatomical image resolution (0.5 × 0.5 × 2 mm) using cubic spline interpolation. This interpolation uses only the data acquired, adding no other information or assumptions, and therefore is completely faithful to the inherent data and resolution of the MRSI. Individual experiments were normalized by the measured polarization. Difference images were calculated as $S_{FID} - 2S_{STEAM}$, where the factor of 2 compensates for the inherent STEAM signal loss. STEAM:control ratios (S_{STEAM}/S_{FID}), used in the analysis were calculated in voxels where the control (FID) acquisition metabolite SNR was greater than 5. Muscle voxels were selected from the mouse back and hip regions.

Results

To illustrate localized metabolite distributions figures 3 and 4 show representative control, STEAM, and difference images in normal and TRAMP mice, respectively. (Note that the coronal slices shown for the TRAMP mice are more anterior than for the normal mice.) The difference image intensity in these figures show where metabolites were attenuated with STEAM MRSI as compared to the FID MRSI. The major vessels through the chest (arrows) as well as the kidneys are particularly well-delineated in Fig. 3a pyruvate and lacatate difference images. The kidneys can also be seen in the TRAMP difference images (Fig. 4). In the STEAM images, primarily alanine was observed in the liver. As expected, the larger encoding strengths lead to greater suppression of all metabolite signals. In the TRAMP tumor regions, there were relatively high lactate levels at both encoding strengths. This was also observed in (40), and is likely due to a higher extra-vascular fraction, either intracellular or in the interstitial space.

Results across all animals, with various STEAM encoding strengths ($\hat{b}$), are summarized in Figure 5 and Table 2. As described in the Methods, we expect differences in the intercept in the exponential fit are primarily due to macroscopic blood flow and bulk motion while differences in $\hat{D}$ are due to microscopic diffusion. Given the 0.125 cm³ size, voxels may include both vasculature and tissue. For comparison, the diffusion coefficients of lactate and alanine in solution at 37°C were measured to be 1.20 and 1.19 × 10⁻³ mm²/s, respectively (47); average ADCs of [3-¹³C]lactate and [3-¹³C]alanine were measured in a rat glioma

model following administration of ^{13}C-labeled glucose to be 0.16 and 0.13×10^{-3} mm[2]/s, respectively (37). (Since pyruvate is almost identical in size to lactate and alanine, we expect it to have a similar ADCs. Intracellular ADCs of metabolites using proton MRSI have been measured to be $\approx 0.1 - 1.0 \times 10^{-3}$ mm[2]/s (32–34).) The fitted effective diffusion coefficients across metabolites and organs (Table 2) were on the order of these previously measured values. They were orders of magnitude smaller than the pseudodiffusion coefficients of macroscopic blood flow, (D^*), for protons (29) supporting our hypothesis that $\hat{D}$ reflects primarily microscopic diffusion. However, they may contain some small contamination from the vascular compartment or motion, as many of the $\hat{D}$ values are greater than the lactate and alanine diffusion coefficients measured in water.

In the prostate tumors, lactate and pyruvate had relatively large intercepts and small $\hat{D}$ compared to other tissues which implies relatively small vascular fractions. This also suggests metabolites in these tumors maybe relatively more intracellular instead of in the interstitial space. Notably, the tumor lactate had the smallest $\hat{D} = 0.24 \times 10^{-3}$ mm[2]/s, which is within the range metabolite intracellular ADCs measured previously. This suggests tumor lactate had the largest intracellular fraction. However, these preliminary fits have low correlation coefficients so further experiments with more quantitative methods are needed to verify this hypothesis. Muscle voxels, measured in the back, also had relatively large intercepts for pyruvate and lactate, implying a small vascular fraction. The kidneys and liver, which are very well perfused organs, had both small intercepts and large $\hat{D}$ for pyruvate and lactate, implying these organs had the largest vascular fractions of these metabolites. However, the liver voxels may also have additional losses in the intercept due to respiratory and cardiac motion.

Of the metabolites, pyruvate had the largest $\hat{D}$ and smallest intercepts, indicating that pyruvate was the most vascular and least intracellular of the metabolites. The large vascular fraction can probably be attributed to the fact that images were acquired only 35 seconds after intravenous pyruvate injection. The large $\hat{D}$ is similar to the metabolite diffusion coefficients in water, which suggests less intracellular pyruvate. This could result from rapid conversion to lactate and alanine once pyruvate is transported into cells. Alanine had the largest intercepts and smallest $\hat{D}$ of the metabolites within the kidneys and liver (alanine SNR in muscle and prostate tumor voxels was not large enough to include). The kidney alanine showed the second smallest $\hat{D} = 0.64 \times 10^{-3}$ mm[2]/s, which is similar to measured intracellular metabolite ADCs. This result especially supports the hypothesis that alanine has a larger intracellular component than the other metabolites, which is expected because the enzyme that generates alanine - alanine aminotransferase (ALT) - is primarily found intracellularly, and alanine is not actively transported out of cells. The $\hat{D}$ of alanine in liver was slightly larger, which could be a result of alanine exported to the liver by other tissues to handle nitrogen disposal.

Discussion

These results confirm that previous observations of elevated conversion from pyruvate to lactate in TRAMP mice tumors (4, 8) were not due to elevated levels of metabolites in the vasculature but were detected by observing tissue metabolites. In fact, these results suggest that the pyruvate to lactate conversion in TRAMP tumors is even more elevated from normal tissues that previously observed. This is because we found larger fractions of vascular metabolites in other organs, which confound the conversion measurements, as compared to the prostate tumors. Thus, the STEAM lactate images show improved delineation of these tumors and could be valuable for improved clinical characterization of cancer.

Overall, the metabolites were highly suppressed for $\hat{b} = 58.4$ s/mm^2, compared to what might be expected from ^{1}H perfusion imaging at $b < 100$ s/mm^2. We believe this is because there was a higher vascular fraction of the ^{13}C metabolites. The pyruvate was injected over 20 sec, including the catheter flush, and the imaging acquisition began 15 sec afterwards. Also, the pyruvate dose used may have saturated the cellular transport (18), especially since the injection resulted in an estimated ≈14.4 mM blood concentration, compared to the ≈80 μM endogenous level. The lactate vascular fraction could be relatively large as well because it is generated by erythrocytes in the blood (16, 17). For example, experiments where a [1-^{13}C]pyruvate bolus was added to whole blood measured a pyruvate-to-lactate LDH-mediated isotope exchange rate of approximately 1.2 1/min = 0.02 1/sec (17), which is on the order of the ≈ 0.06 1/sec rates measured in lymphoma tumors (5). The supraphysiologic pyruvate bolus used in these studies may have saturated the LDH activity, unlike the whole blood studies that used a much smaller bolus, which would reduce the blood exchange rate.

One disadvantage of the presented STEAM MRSI approach is that only a single 90-90 encoding step is feasible because the entire hyperpolarized magnetization is used, which makes the experiment sensitive to the timing of the encoding and elminates the possibility of dynamic imaging. One possible solution would be to monitor the bolus arrival and then perform the STEAM acquisition at a fixed time after the pyruvate peak. Other approaches using outer volume saturation pulses (20) or subsequent gadolinium injections (21) will create unnecessary signal loss if the saturation or gadolinium is applied prior to tissue perfusion, but images can be acquired dynamically with these approaches to measure kinetics.

Another disadvantage of STEAM MRSI is the signal loss due to bulk motion between the encoding and acquisition. Since this study was performed, we designed a stimulated-echo preparation approach, in which the encoding gradients are rephased and thus motion sensitivity is halted prior to the acquisition (40). STEAM combined with faster imaging techniques, such as spiral CSI (48) and metabolite specific-imaging (49), could also help reduce this blurring, as would several other perfusion-sensitive approaches (20–22).

Figure 5 shows the relatively high variability across all of our experiments, which can come from (1) inter-animal variation (fits were performed across different animals) and (2) inter-experiment variations (ratios were computed from two separate pyruvate injections). Likely causes include physiologic differences, varying polarization levels, spontaneous emission of signal and loss of polarization (50), and RF calibration errors (STEAM is more sensitive than spin-echo or gradient-echo imaging to RF inhomogeneity). The inter-experiment variability and limited number of injections that can be performed currently limits the degree of quantitative perfusion and diffusion measurements that can be performed using this imaging method. New methods must be developed for future studies to reduce this variability and enable quantitation, such as acquiring multiple b-value images following a single injection.

Conclusion

We have demonstrated perfusion and diffusion-sensitive MRSI *in vivo* following injection of hyperpolarized [1-^{13}C]pyruvate with multiple encoding strengths. Vascular metabolites were preferentially suppressed at all encoding strengths compared to those generated from metabolic conversion occurring in tissue, which had the result of improved contrast for the cancer biomarker lactate in the TRAMP model prostate tumors. Using a multiple $\hat{b}$-value acquisitions across different animals enabled us to roughly estimate relative perfusion and vascular fractions as well as effective diffusion coefficients, $\hat{D}$. The measured $\hat{D}$ were in a

reasonable range between the free water diffusion coefficients and intracellular ADCs of metabolites. Future studies with improved methods for hyperpolarized ^{13}C metabolic imaging are required to better quantitate ADCs and vascular fractions for individual subjects, as well to validate the initial findings presented. In studies of the TRAMP prostate tumor mouse model, we observed that the lactate and pyruvate in prostate tumors had smaller vascular fractions and were likely more intracellular. In the well-vascularized kidneys and liver, there was a larger vascular fraction of pyruvate and lactate when compared to muscle and prostate tumor tissue. Pyruvate - the injected substrate - had a larger vascular fraction than its metabolic products of lactate and alanine. Our results also indicated that alanine had the largest extravascular fraction. These results show the potential value of STEAM MRSI in tumor metabolic imaging for suppression of the vascular signal, which can contaminate evaluation of the metabolic profile in tumor voxels, and highlighting of the abnormal metabolism in cancer.

Acknowledgments

References

1. Ardenkjaer-Larsen JH, Fridlund B, Gram A, Hansson G, Hansson L, Lerche MH, Servin R, Thaning M, Golman K. Increase in signal-to-noise ratio of > 10,000 times in liquid-state NMR. Proc Natl Acad Sci U S A. 2003; 100:10158–10163. [PubMed: 12930897]

2. Golman K, Ardenkjaer-Larsen JH, Petersson JS, Mansson S, Leunbach I. Molecular imaging with endogenous substances. Proc Natl Acad Sci U S A. 2003; 100:10435–10439. [PubMed: 12930896]

3. Golman K, in't Zandt R, Thaning M. Real-time metabolic imaging. Proc Natl Acad Sci U S A. 2006; 103:11270–11275. [PubMed: 16837573]

4. Chen AP, Albers MJ, Cunningham CH, Kohler SJ, Yen YF, Hurd RE, Tropp J, Bok R, Pauly JM, Nelson SJ, Kurhanewicz J, Vigneron DB. Hyperpolarized C-13 spectroscopic imaging of the TRAMP mouse at 3T–initial experience. Magn Reson Med. 2007; 58:1099–1106. [PubMed: 17969006]

5. Day SE, Kettunen MI, Gallagher FA, Hu DE, Lerche M, Wolber J, Golman K, Ardenkjaer-Larsen JH, Brindle KM. Detecting tumor response to treatment using hyperpolarized ^{13}C magnetic resonance imaging and spectroscopy. Nat Med. 2007; 13:1382–1387. [PubMed: 17965722]

6. Merritt ME, Harrison C, Storey C, Jeffrey FM, Sherry AD, Malloy CR. Hyperpolarized 13C allows a direct measure of flux through a single enzyme-catalyzed step by NMR. Proc Natl Acad Sci U S A. 2007; 104:19773–19777. [PubMed: 18056642]

7. Merritt ME, Harrison C, Storey C, Sherry AD, Malloy CR. Inhibition of carbohydrate oxidation during the first minute of reperfusion after brief ischemia: NMR detection of hyperpolarized ^{13}CO$_2$ and H13CO3- Magn Reson Med. 2008; 60:1029–36. [PubMed: 18956454]

8. Albers MJ, Bok R, Chen AP, Cunningham CH, Zierhut ML, Zhang VY, Kohler SJ, Tropp J, Hurd RE, Yen YF, Nelson SJ, Vigneron DB, Kurhanewicz J. Hyperpolarized C-13 lactate pyruvate, and alanine: Noninvasive biomarkers for prostate cancer detection and grading. Cancer Res. 2008; 68:8607–8615. [PubMed: 18922937]

9. Schroeder MA, Cochlin LE, Heather LC, Clarke K, Radda GK, Tyler DJ, Shulman RG. In vivo assessment of pyruvate dehydrogenase flux in the heart using hyperpolarized carbon-13 magnetic resonance. Proc Natl Acad Sci U S A. 2008; 105:12051–12056. [PubMed: 18689683]

10. Witney TH, Kettunen MI, De Hu, Gallagher FA, Bohndiek SE, Napolitano R, Brindle KM. Detecting treatment response in a model of human breast adenocarcinoma using hyperpolarised [1-13c]pyruvate and [1,4-13c2]fumarate. Br J Cancer. 2010; 103:1400–6. [PubMed: 20924379]

11. Park I, Larson PEZ, Zierhut ML, Hu S, Bok R, Ozawa T, Kurhanewicz J, Vigneron DB, VandenBerg SR, James CD, Nelson SJ. Hyperpolarized 13C MR metabolic imaging: application to brain tumors. Neuro Oncol. 2010; 12:133–44. [PubMed: 20150380]

12. Darpolor MM, Yen YF, Chua MS, Xing L, ClarkeKatzenberg RH, Shi W, Mayer D, Josan S, Hurd RE, Pfefferbaum A, Senadheera L, So S, Hofmann LV, Glazer GM, Spielman DM. In vivo mrsi of hyperpolarized [1-(13)c]pyruvate metabolism in rat hepatocellular carcinoma. NMR Biomed. 2011; 24:506–513. [PubMed: 21674652]

13. MacKenzie JD, Yen YF, Mayer D, Tropp J, Hurd R, Spielman DM. Detection of inflammatory arthritis using hyperpolarized 13c-pyurvate with magnetic resonance imaging and spectroscopy. Radiology. 2011; 259:414–420. [PubMed: 21406626]

14. Kurhanewicz J, Vigneron DB, Brindle K, Chekmenev EY, Comment A, Cunning-ham CH, DeBerardinis RJ, Green GG, Leach MO, Rajan SS, Rizi RR, Ross BD, Warren WS, Malloy CR. Analysis of cancer metabolism by imaging hyperpolarized nuclei: Prospects for translation to clinical research. Neoplasia. 2011; 13:81–97. [PubMed: 21403835]

15. Pullinger B, Profka H, ArdenkjaerLarsen JH, Kuzma NN, Kadlecek S, Rizi RR. Metabolism of hyperpolarized [1-(13) c]pyruvate in the isolated perfused rat lung -an ischemia study. NMR Biomed. 2012; 25:1113–8. [PubMed: 22311307]

16. Brindle KM, Campbell ID, Simpson RJ. A 1h-nmr study of the activity expressed by lactate dehydrogenase in the human erythrocyte. Eur J Biochem. 1986; 158:299–305. [PubMed: 3732272]

17. Romijn JA, Chinkes DL, Schwarz JM, Wolfe RR. Lactate-pyruvate interconversion in blood: implications for in vivo tracer studies. Am J Physiol. 1994; 266:E334–40. [PubMed: 8166253]

18. Harris T, Eliyahu G, Frydman L, Degani H. Kinetics of hyperpolarized 13C1-pyruvate transport and metabolism in living human breast cancer cells. Proc Natl Acad Sci U S A. 2009; 106:18131–6. [PubMed: 19826085]

19. Keshari KR, Kurhanewicz J, Jeffries RE, Wilson DM, Dewar BJ, Criekinge MV, Zierhut M, Vigneron DB, Macdonald JM. Hyperpolarized (13)C spectroscopy and an NMR-compatible bioreactor system for the investigation of real-time cellular metabolism. Magn Reson Med. 2010; 63:322–329. [PubMed: 20099325]

20. Chen AP, Leung K, Lam W, Hurd RE, Vigneron DB, Cunningham CH. Design of spectral-spatial outer volume suppression rf pulses for tissue specific metabolic characterization with hyperpolarized 13c pyruvate. J Magn Reson. 2009; 200:344–8. [PubMed: 19616981]

21. Smith M, Peterson E, Gordon J, Niles D, Rowland I, Kurpad K, Fain S. In-vivo imaging and spectroscopy of dynamic metabolism using simultaneous 13c and 1h mri. IEEE Trans Biomed Eng. 2012; 59, 1:45–49. [PubMed: 21775254]

22. Josan S, Yen YF, Hurd R, Pfefferbaum A, Spielman D, Mayer D. Application of double spin echo spiral chemical shift imaging to rapid metabolic mapping of hyperpolarized [1-(13)c]-pyruvate. Journal of Magnetic Resonance. 2011; 209:332–336. [PubMed: 21316280]

23. Frahm J, Hänicke W, Bruhn H, Gyngell ML, Merboldt KD. High-speed STEAM MRI of the human heart. Magn Reson Med. 1991; 22:133–142. [PubMed: 1798388]

24. Fischer SE, Stuber M, Scheidegger MB, Boesiger P. Limitations of stimulated echo acquisition mode (STEAM) techniques in cardiac applications. Magn Reson Med. 1995; 34:80–91. [PubMed: 7674902]

25. Tanner JE. Use of the stimulated echo in NMR diffusion studies. J Chem Phys. 1970; 52:2523–6.

26. Merboldt KD, Hänicke W, Frahm J. Diffusion imaging using stimulated echoes. Magn Reson Med. 1991; 19:233–9. [PubMed: 1881309]

27. Frahm J, Bruhn H, Gyngell ML, Merboldt KD, Hänicke W, Sauter R. Localized high-resolution proton nmr spectroscopy using stimulated echoes: initial applications to human brain in vivo. Magn Reson Med. 1989; 9:79–93. [PubMed: 2540396]

28. Bihan DL, Breton E, Lallemand D, Grenier P, Cabanis E, LavalJeantet M. MR imaging of intravoxel incoherent motions: application to diffusion and perfusion in neurologic disorders. Radiology. 1986; 161:401–7. [PubMed: 3763909]

29. Bihan DL, Breton E, Lallemand D, Aubin ML, Vignaud J, LavalJeantet M. Separation of diffusion and perfusion in intravoxel incoherent motion MR imaging. Radiology. 1988; 168:497–505. [PubMed: 3393671]

30. Tanner J. Intracellular diffusion of water. Archives of Biochemistry and Biophysics. 1983; 224:416–428. [PubMed: 6347071]

31. VanZijl PC, Moonen CT, Faustino P, Pekar J, Kaplan O, Cohen JS. Complete separation of intracellular and extracellular information in nmr spectra of perfused cells by diffusion-weighted spectroscopy. Proceedings of the National Academy of Sciences. 1991; 88:3228–3232.

32. Pilatus U, Shim H, Artemov D, Davis D, VanZijl PCM, Glickson JD. Intracellular volume and apparent diffusion constants of perfused cancer cell cultures, as measured by nmr. Magnetic Resonance in Medicine. 1997; 37:825–832. [PubMed: 9178232]

33. Pfeuffer J, Flšgel U, Dreher W, Leibfritz D. Restricted diffusion and exchange of intra-cellular water: theoretical modelling and diffusion time dependence of 1h nmr measurements on perfused glial cells. NMR in Biomedicine. 1998; 11:19–31. [PubMed: 9608585]

34. Pfeuffer J, Tkác I, Gruetter R. Extracellular-intracellular distribution of glucose and lactate in the rat brain assessed noninvasively by diffusion-weighted 1h nuclear magnetic resonance spectroscopy in vivo. J Cereb Blood Flow Metab. 2000; 20:736–46. [PubMed: 10779018]

35. Mardor Y, Kaplan O, Sterin M, RuizCabello J, Ash E, Roth Y, Ringel I, Cohen JS. Noninvasive real-time monitoring of intracellular cancer cell metabolism and response to lonidamine treatment using diffusion weighted proton magnetic resonance spectroscopy. Cancer Research. 2000; 60:5179–5186. [PubMed: 11016646]

36. Nicolay K, Braun KPJ, Graaf RAd, Dijkhuizen RM, Kruiskamp MJ. Diffusion nmr spectroscopy. NMR in Biomedicine. 2001; 14:94–111. [PubMed: 11320536]

37. Pfeuffer J, Lin JC, Delabarre L, Ugurbil K, Garwood M. Detection of intracellular lactate with localized diffusion 1H-13C-spectroscopy in rat glioma in vivo. J Magn Reson. 2005; 177:129–38. [PubMed: 16111904]

38. Zhao L, Sukstanskii AL, Kroenke CD, Song J, PiwnicaWorms D, Ackerman JJH, Neil JJ. Intracellular water specific mr of microbead-adherent cells: Hela cell intracellular water diffusion. Magnetic Resonance in Medicine. 2008; 59:79–84. [PubMed: 18050315]

39. Chen AP, Hurd RE, Cunningham CH. Spin tagging for hyperpolarized 13c metabolic studies. Journal of Magnetic Resonance. 2012; 214:319–323. [PubMed: 22050921]

40. Larson PEZ, Kerr AB, Reed GD, Hurd RE, Kurhanewicz J, Pauly JM, Vigneron DB. Generating super stimulated-echoes in MRI and their application to hyperpolarized C-13 diffusion metabolic imaging. IEEE Trans Med Imaging. 2012; 31:265–275. [PubMed: 22027366]

41. Frahm J, Haase A, Matthei D, Merboldt KD, Hänicke W. Rapid NMR imaging using stimulated echoes. J Magn Reson. 1985; 65:130–135.

42. Zhao L, Mulkern R, Tseng CH, Williamson D, Patz S, Kraft R, Walsworth RL, Jolesz FA, Albert MS. Gradient-echo imaging considerations for hyperpolarized ^{129}Xe MR. J Magn Reson B. 1996; 113:179–183.

43. Yen YF, Kohler SJ, Chen AP, Tropp J, Bok R, Wolber J, Albers MJ, Gram KA, Zierhut ML, Park I, Zhang V, Hu S, Nelson SJ, Vigneron DB, Kurhanewicz J, Dirven HA, Hurd RE. Imaging considerations for in vivo (13)C metabolic mapping using hyperpolarized (13)C-pyruvate. Magn Reson Med. 2009; 62:1–10. [PubMed: 19319902]

44. Derby K, Tropp J, Hawryszko C. Design and evaluation of a novel dual-tuned resonator for spectroscopic imaging. J Magn Reson. 1990; 86:256–262.

45. Hu, S.; Larson, PE.; VanCriekinge, M.; Leach, AM.; Park, I.; Shin, PJ.; Reed, G.; Yoshihara, H.; Bok, RA.; Nelson, SJ.; Kurhanewicz, J.; Vigneron, DB. Rapid sequential injections of hyperpolarized [1-13c]pyruvate in vivo using a sub-kelvin, multi-sample dnp polarizer. Proc ISMRM 20th Annual Meeting; Melbourne, Australia. 2012; p. 4303

46. Yen, YF.; Roux, PL.; Bok, R.; Tropp, J.; Chen, AP.; Zhang, V.; Zierhut, ML.; Albers, M.; Park, I.; Nelson, SJ.; Vigneron, DB.; Kurhanewicz, J.; Hurd, RE. Apparent T_2 of ^{13}C-labeled metabolites in vivo. Proceedings of the 16th Annual Meeting of ISMRM; Toronto. 2008. p. 1747

47. Lundberg P, Kuchel PW. Diffusion of solutes in agarose and alginate gels: 1h and 23na pfgse and 23na tqf nmr studies. Magn Reson Med. 1997; 37:44–52. [PubMed: 8978631]

48. Mayer D, Yen YF, Tropp J, Pfefferbaum A, Hurd RE, Spielman DM. Application of subsecond spiral chemical shift imaging to real-time multislice metabolic imaging of the rat in vivo after

injection of hyperpolarized 13C1-pyruvate. Magn Reson Med. 2009; 62:557–64. [PubMed: 19585607]

49. Cunningham CH, Chen AP, Lustig M, Hargreaves BA, Lupo J, Xu D, Kurhanewicz J, Hurd RE, Pauly JM, Nelson SJ, Vigneron DB. Pulse sequence for dynamic volumetric imaging of hyperpolarized metabolic products. J Magn Reson. 2008; 193:139–146. [PubMed: 18424203]

50. Chen HY, Lee Y, Bowen S, Hilty C. Spontaneous emission of nmr signals in hyperpolarized proton spin systems. J Magn Reson. 2011; 208:204–9. [PubMed: 21145766]
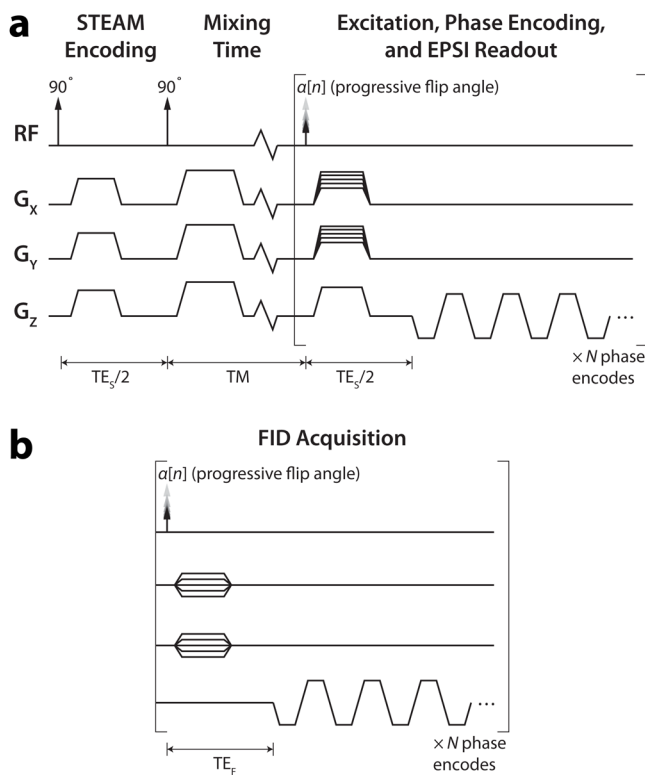
Figure 1.
(a) 3D STEAM MRSI pulse sequence for hyperpolarized substrates. A single stimulated-echo encoding step is used, followed by a series of excitations and readouts to acquire a 3D MRSI. (b) FID MRSI pulse sequence used for Control studies. The excitation flip angle, $a[n]$, is incremented to efficiently utilize all of the magnetization (42).
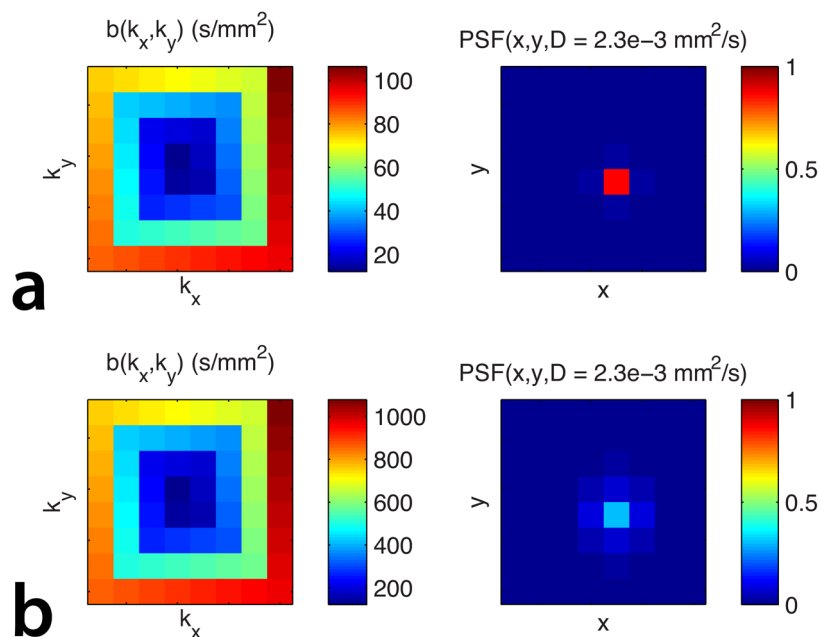
Figure 2.
Point spread function (PSF) analysis of $b(\vec{k})$ for concentric phase encode ordering used to characterize the diffusion-weighting. The ideal PSF is a delta-function with an amplitude of 1, which the diffusion-weighting decreases. (a) Smaller encoding strength weighting, for which the effective b-value is $\hat{b} = 58.4$. (b) Larger encoding strength weighting, for which the effective b-value is $\hat{b} = 513.3$.
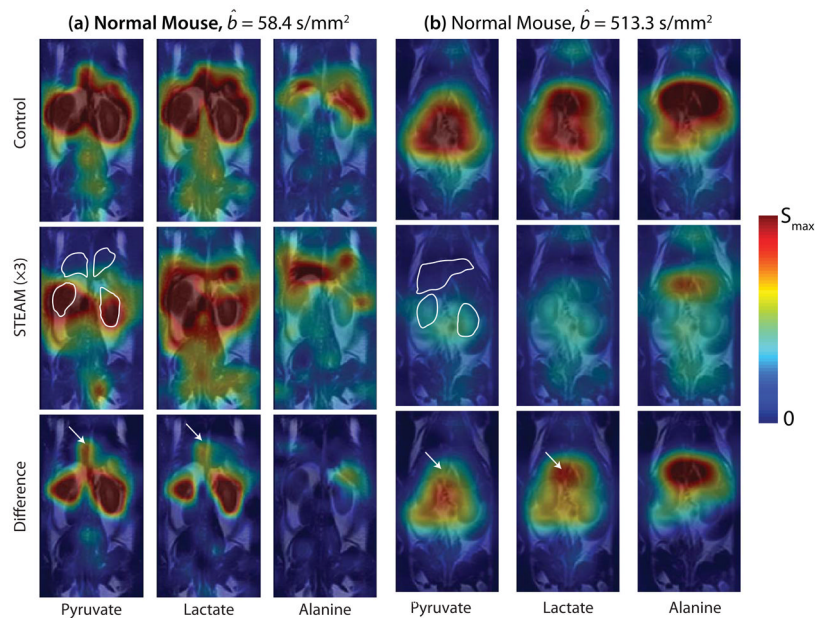
(a) Normal Mouse, $\hat{b} = 58.4$ s/mm² **(b) Normal Mouse,** $\hat{b} = 513.3$ s/mm²

Figure 3.
Representative STEAM contrast images in normal mice at different encoding strengths. White outlines are drawn around the liver and kidneys in the pyruvate STEAM images. The kidneys and major vasculature (arrows) are bright in the pyruvate and lactate Difference images. Alanine is seen primarily near the liver. The higher encoding strength reduces the signal substantially for all metabolites.
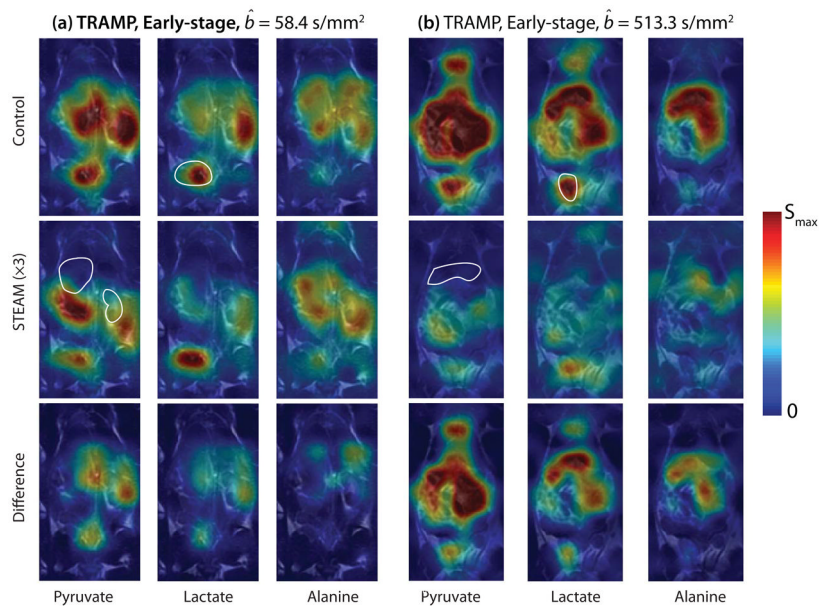
(a) TRAMP, Early-stage, $\hat{b}$ = 58.4 s/mm²   (b) TRAMP, Early-stage, $\hat{b}$ = 513.3 s/mm²

Control   STEAM (×3)   Difference

Pyruvate   Lactate   Alanine   Pyruvate   Lactate   Alanine

S_{max} 0

Figure 4.
Representative STEAM contrast images in TRAMP mice at different encoding strengths. White outlines are drawn around the liver and kidneys in the pyruvate STEAM images, and the prostate tumors in the lactate Control images. Note that these coronal images show more anterior slices than Fig. 3, although the left kidneys can still be seen in (a) with high intensity in the pyruvate and lactate difference images. The prostate tumors (outlined in Control lactate images) have relatively high lactate and pyruvate in both the control and STEAM images for both encoding strengths, while the difference images, particularly at the larger $\hat{b}$, have more metabolites outside of the tumors.
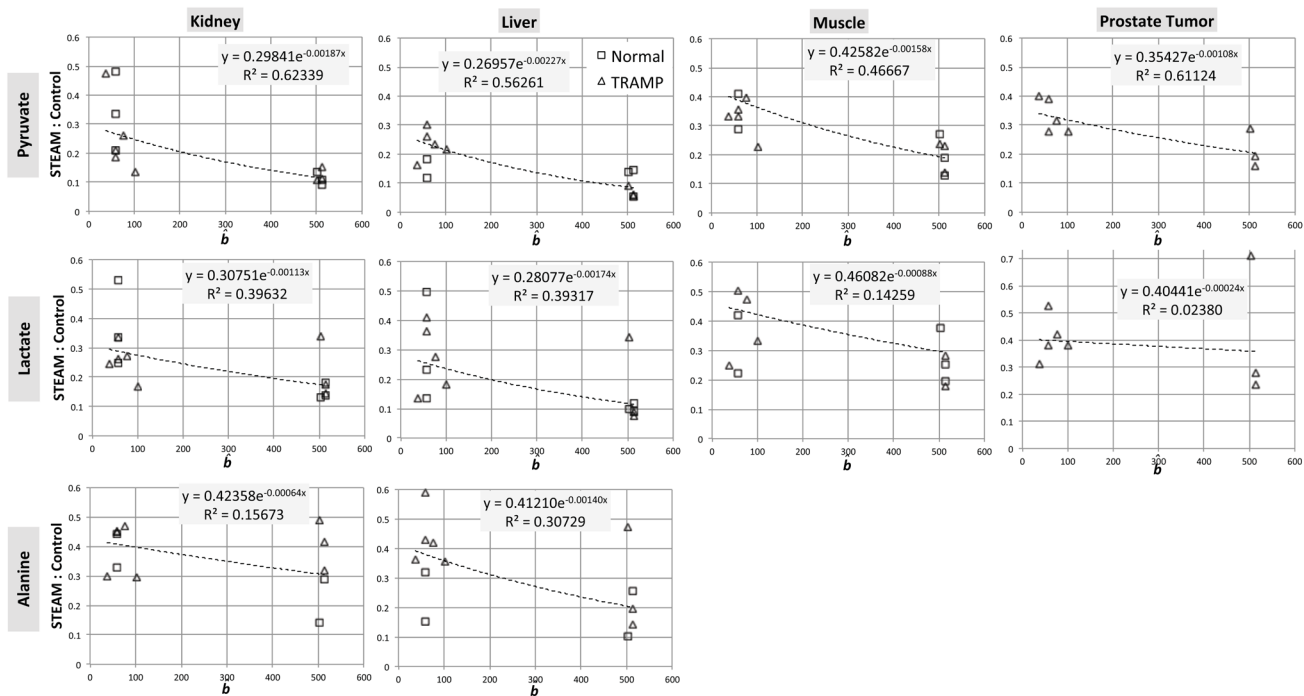
Figure 5.
STEAM:control ratios across all 14 mice - 6 normal (□), 8 TRAMP (▲). The dashed lines
are exponential regression fits to the data based on the model in Eq. 7, and the fit values are
in Table 2. These results provide preliminary insight into the vascular, interstitial, and
intracellular compartmentalization. However, the power of these results is limited, as shown
by the poor fit quality (low R^2). This is likely a result of (1) individual variations when
comparing across different animals and (2) quantitative limitations when using two separate
pyruvate injections to estimate the STEAM suppression.

Table 1

STEAM experimental encoding strength parameters.

TM (s)	δ (ms)	G_{STEAM} (G/cm)	$\hat{b}$ (s/mm^2)
1	2.7	1.9	58.4
1	2.7	6.1	513.3
2	0.72	5.2	37.5
3	0.72	6.9	76.9
6	2.5	1.9	101.0
1	8.5	1.9	501.6

Table 2

Exponential fits to Equation 7 for the metabolite and tissue data shown in Figure 5.

		Kidneys	Liver	Muscle	Prostate Tumor
Intercept	Pyruvate	0.30	0.27	0.43	0.35
	Lactate	0.31	0.28	0.46	0.40
	Alanine	0.42	0.41		
$\hat{D}\,(\times 10^{-3}\ \text{mm}^2/\text{s})$	Pyruvate	1.87	2.27	1.58	1.08
	Lactate	1.13	1.74	0.88	0.24
	Alanine	0.64	1.40		